



## Small molecular hole-transporting and emitting materials for hole-only green organic light-emitting devices



Xicheng Liu <sup>a, b, d</sup>, Junfei Liang <sup>c</sup>, Jing You <sup>a, b, \*</sup>, Lei Ying <sup>c</sup>, Yin Xiao <sup>a, b</sup>, Shirong Wang <sup>a, b</sup>, Xianggao Li <sup>a, b</sup>

<sup>a</sup> Tianjin University, School of Chemical Engineering and Technology, Tianjin, 300072, China

<sup>b</sup> Collaborative Innovation Center of Chemical Science and Engineering, Tianjin, 300072, China

<sup>c</sup> South China University of Technology, State Key Laboratory of Luminescent Materials and Devices, Guangzhou, 510640, China

<sup>d</sup> Qufu Normal University, School of Chemistry and Chemical Engineering, Qufu, 273165, China

### ARTICLE INFO

#### Article history:

Received 20 December 2015

Received in revised form

28 March 2016

Accepted 29 March 2016

Available online 30 March 2016

#### Keywords:

Triphenylamine

Hole-transporting materials

Hole-only

Simple-structured

Fully solution-processed

Organic light-emitting diodes

### ABSTRACT

Three small molecular hole-transporting and emitting materials with naphthalene bridged triphenylamine or carbazole were synthesized. These compounds exhibited high absolute fluorescence quantum yields (70–88%) at the green light region (540–555 nm), suitable highest occupied molecular orbital levels (−5.26 ~ −5.34 eV) and good hole mobilities ( $\sim 10^{-4}$  cm<sup>2</sup> V<sup>-1</sup> s<sup>-1</sup>). The hole-only organic light emitting diodes with as-synthesized hole-transporting and emitting materials showed a tune-on voltage and a maximum brightness of 2.6 V and 2010 cd m<sup>-2</sup>, respectively. Three stages of voltage-dependent current were observed, which coincide with the characteristic of Ohmic current, Fowler-Nordheim current and space charge limited current. With analysis of above models, overlarge Fowler-Nordheim current and space charge limited current contribute to the low efficiency of the device. All these results indicated that the high hole mobility showed the negative effect on the device efficiency, especially at high operation voltage.

© 2016 Published by Elsevier Ltd.

### 1. Introduction

The research on multilayer organic light-emitting diodes (OLEDs) is dominant in recent decades for the outstanding performance [1,2]. While, simplifying device structure is still regarded as one of the most important solution for low cost OLEDs [3,4]. This requires that the material of active layer should be multifunctional with charge transfer and light emission. In earlier studies, 8-hydroxyquinoline aluminum (Alq<sub>3</sub>) derivatives were applied as emitting and electron-only OLEDs fabricated with vacuum thermal deposition, which showed poor performance of 210 cd m<sup>-2</sup> at 15 V and the highest current efficiency reached 0.17 cd A<sup>-1</sup> at 40 cd m<sup>-2</sup> [5,6]. The solution-processed OLEDs with hole-transporting character mainly refer to electroluminescence polymer, such as poly(*p*-phenylene vinylene) (PPV) [7]. However, the uncertain molecular structure and weight of polymer lead to the complicated synthesis and purification processes. Therefore, the simple-structured small

molecule OLEDs (SMOLEDs) with solution process has become an exciting way for the development of OLEDs [8,9].

As reported, the triphenylamine (TPA) and carbazole (Cz) derivatives have been normally used as small molecular hole-transporting materials (HTMs) [10–14]. Previously, our group have reported a series of TPA based HTMs with outstanding film-forming character [15,16]. In addition, TPA and Cz based materials with  $\pi$ -conjugation bridge showed excellent performance as fluorescence emission materials [17,18], such as 4,4'-di-2-(4-*N,N'*-diphenylamino phenyl vinyl biphenyl) (DPAVBi) and 4,4'-bis((*E*)-2-(9-ethyl-9*H*-carbazol-3-yl) vinyl)-1,1'-biphenyl (BCzVBi), which were widely used in multilayer blue OLEDs.

To these viewpoints, three small molecular hole-transporting and emitting materials (HT-EMs) with naphthalene bridged TPA or Cz were synthesized (Molecular structures see Fig. 1, synthesis routes see ESI Scheme S1). These as-synthesized HT-EMs showed hole mobility ( $\mu_h$ ) of  $4.03 \times 10^{-4}$ ,  $4.22 \times 10^{-4}$  and  $3.24 \times 10^{-4}$  cm<sup>2</sup> V<sup>-1</sup> s<sup>-1</sup> at the electric field of  $\sim 1.5 \times 10^5$  V cm<sup>-1</sup>, respectively. Fully solution-processed simple-structured OLEDs (Poly(3,4-ethylene-dioxythiophene) poly(styrenesulfonate) (PEDOT:PSS) and poly[(9,9-bis(3'-(*N,N*-dimethylamino)propyl)-

\* Corresponding author. Tianjin University, School of Chemical Engineering and Technology, Tianjin, 300072, China.

E-mail address: [Youj1983@tju.edu.cn](mailto:Youj1983@tju.edu.cn) (J. You).

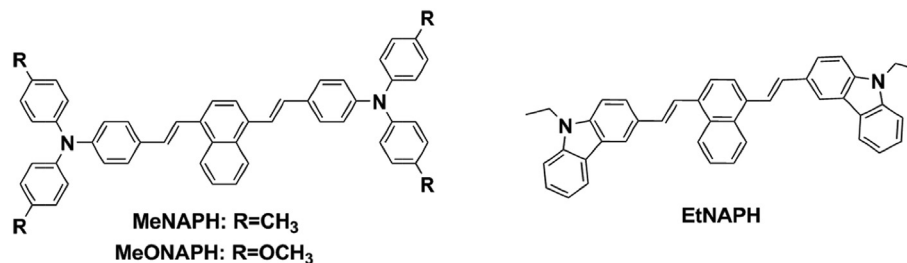


Fig. 1. Molecular structures of as-synthesized HT-EMs.

2,7-fluorene)-alt-2,7-(9,9-dioctylfluorene)] (PFN) were applied as the electrode modified materials, HT-EMs as light-emitting materials) were fabricated and showed tune-on voltages, the maximum brightness, maximum luminance efficiency and external quantum efficiency were 2.6 V, 2010 cd m<sup>-2</sup>, 0.65 cd A<sup>-1</sup> and 0.25%, respectively. In this kind of device, three stages have been observed in the *J*-*V* curves based on different operation voltage, which showed a feature of Ohmic type current (*J*<sub>ohmic</sub>), Fowler-Nordheim type current (*J*<sub>FN</sub>) and space charge limited type current (*J*<sub>SCLC</sub>). In the second and third stages, the *J*<sub>FN</sub> and *J*<sub>SCLC</sub> showed a directly proportional to  $\mu_h$ . In this work, the hole mobility showed an negative effect on the efficiency in simple-structured device. An equilibrium of carrier transfer plays a key role in achieving high performance in simple-structured OLEDs.

## 2. Experimental section

### 2.1. General information

1,4-naphthalenedicarboxylic acid, poly(3,4-ethylene-dioxythiophene) poly(styrenesulfonate) (PEDOT:PSS) and Aluminum (Al, 99%) were purchased from Tianjin Heowns Biochemical Technology Co. Ltd. (Tianjin, China), other reagents were purchased from Tianjin Guangfu Fine Chemical Research Institute (Tianjin, China). Indium-tin-oxide (ITO) glasses were purchased from South China Xiangcheng Technology Co. Ltd. (Shenzhen, China). Poly[(9,9-bis(3'-(*N,N*-dimethylamino)propyl)-2,7-fluorene)-alt-2,7-(9,9-dioctyl fluorene)] (PFN) was provided by South China University of Technology. Tetrahydrofuran (THF) was distilled before use. All the other agents were used without further treatments.

As-synthesized HT-EMs were identified by nuclear magnetic resonance (NMR) and mass spectroscopies (MS). The NMR were recorded on a Bruker AVANCE III 400 MHz spectrometer, with the chemical shifts reported in ppm using tetramethylsilane (TMS) as an internal standard. MS was recorded on a LCQ Advantage MAX mass spectrometer. Ultraviolet–visible absorption (UV–Vis) and photoluminescence (PL) spectra were obtained on the Thermo Evolution 300 UV–Visible spectrometer and a Cary Eclipse fluorescence spectrometer, respectively. Fluorescence lifetime was obtained by FluoroLog 3 Steady transient fluorescence test system. Fluorescence quantum yields were obtained on a Varian Cary Eclipse test system. Decomposition temperature (*T*<sub>d</sub>) and glass transition temperature (*T*<sub>g</sub>) were determined by the thermal gravimetric analysis (TGA) and differential scanning calorimeter (DSC) on a TA Q500 thermo gravimetric analysis under nitrogen atmosphere. The photoelectron yield spectroscopy (PYS) was carried out on the Sumitomo PYS-202 ionization energy detection system. The morphology of solid film was characterized by a Rigaku Miniflex 600 X-Ray diffraction (XRD) and Nanosurf AG Easyscan 2 atomic force microscopy (AFM).

Crystal structure of MeNAPH was obtained by Smart Apex X-Ray single crystal diffraction. X-Ray crystallography of MeNAPH were

recorded with the graphine monochromated Mo-*K* $\alpha$  radiation ( $\lambda = 0.71073$  Å) on a Bruker P4 four-circle diffractometer. The structure was solved with a SHELXS-97 program [19]. Non-hydrogen atoms were located in successive difference Fourier syntheses. The final refinement was performed by full matrix least-squares methods with anisotropic parameters for nonhydrogen atoms on *F*<sup>2</sup> using the SHELXTL and ORTEP software [20]. Crystallographic data reported in this paper had been deposited with the Cambridge Crystal Data Centre and CCDC No. 1413201.

The time-of-flight (TOF) measurement was recorded on a TOF401 (Sumitomo Heavy Industries, Ltd., Japan). Samples were prepared through vacuum deposition with a structure of ITO/HT-EMs (~1  $\mu$ m)/Al (100 nm) and an active area of 4 × 4 mm<sup>2</sup>.

### 2.2. Quantum chemical calculation

Quantum chemical calculation was performed on a Gaussian 03 program with the Beck's three-parameter exchange functional and the Lee-Yang-Parr's correlation functional (B3LYP) using 6-31G (d) basis sets [21].

### 2.3. OLED fabrication and measurements

ITO glasses (sheet resistance: 10  $\Omega$ /square) were cleaned with following sequence: acetone, methanol and diluted water, then annealed at 120 °C for 20 min followed by O<sub>2</sub> plasma treatment [22]. An anode modified layer (~20 nm) was achieved by spin-coating the PEDOT: PSS colloidal solution on the ITO side at 3000 rpm, then baked at 120 °C for 30 min. The 20 mg mL<sup>-1</sup> concentrated HT-EMs THF solutions were spin-coated on the PEDOT:PSS film at 2000 rpm, and 80 nm thick HT-EMs were achieved after baking at 80 °C for 30 min. The cathode modified layer of PFN (~20 nm) was deposited by spin-coating at 3000 rpm, followed by baking at 80 °C for 20 min. A 100 nm thickness of Al was thermally deposited as a cathode under vacuum at a base pressure <1 × 10<sup>-4</sup> Pa, monitored by the Sycon STM-100 crystal thickness meter. The thicknesses of all spin-coated films were measured by the TencorAlfa Step-500 terrace detector. The active area of the device is 4 × 4 mm<sup>2</sup>, determined by the cross breadth between the cathode (Al) and the anode (ITO). The EL spectra was measured by the SpectrScan PR705 spectra. Steady current-luminance-voltages were measured by the Keithley 236 with silicon photodiode. All tests were performed under air atmosphere at room temperature.

## 3. Results and discussions

### 3.1. Molecular structures and energy levels

The as-synthesized HT-EMs were synthesized by Wittig reaction (ESI Scheme S1). The HT-EMs are soluble in common organic solvents such as toluene, tetrahydrofuran, chloroform and chlorobenzene, which ensure they can be deposited with solution

processes [23]. The HT-EMs exhibit good thermal stability with decomposition temperatures ( $T_d$ ) in the range of 420–460 °C and glass transition temperatures ( $T_g$ ) in the range of 91.2–117.3 °C for MeNAPH, MeONAPH and EtNAPH, respectively (ESI Fig. S3 and Table S2).

The normalized UV–Vis absorption and photoluminescence (PL) spectra of as-synthesized HT-EMs in THF solution ( $1.0 \times 10^{-5}$  mol L<sup>-1</sup>) and spin-coated films are shown in Fig. 2, relevant data are summarized in Table 1.

As shown in Fig. 2, these HT-EMs show two absorption regions in 300–310 nm and 400–450 nm. The absorption region in 300–310 nm can be assigned to the  $n-\pi^*$  transition of the TPA moieties. The absorption region in 400–450 nm attributes to the intramolecular charge transfer (ICT) of  $\pi-\pi^*$  transition [24,25]. The maximum absorption peak ( $\lambda_{\text{abs}/\text{max}}$ ) of EtNAPH showed a blue shift compared with MeNAPH and MeONAPH. Similar phenomenon also can be observed in the fluorescence emission spectra of solutions (Fig. 2a) because of the larger conjugated degree of MeNAPH and MeONAPH than EtNAPH. The UV–Vis and PL spectra of the thin films display a similar pattern as those of the solutions for MeNAPH and MeONAPH, which indicates that no significant aggregation or crystallization occurs in the solid films [26]. Serious intermolecular stacking is observed in EtNAPH leading to the red shift of emission peak in film [27].

The energy levels and the corresponding frontier orbital distributions were calculated by DFT method. The highest occupied molecular orbital (HOMO) levels, lowest unoccupied molecular orbital (LUMO) energy levels and the energy gap ( $E_g$ ) are shown in Fig. 3. These results agreed well with the tendency determined by photoelectron yield spectroscopy (PYS, ESI Fig. S4) [28,29] and optical measurements (Fig. 2).

As shown in Table 1, MeONAPH has the longest fluorescence lifetime ( $\tau$ , ESI Fig. S5) and highest quantum efficiency ( $\phi_f$ ).

The dihedral angle ( $\theta$ ) between P1 and P2 of the benzene ring in triphenylamine or carbazole units connecting with naphthalene are 39.5° and 39.3° for MeNAPH and MeONAPH in optimized structure (ESI Fig. S6). This indicates that the MeNAPH and MeONAPH show better molecular planarity and larger  $\pi$  conjugated degree than EtNAPH in which the dihedral between carbazole and naphthalene is 44.5°. This resulted in the red-shifted of emission and the improvement of  $\tau$  and  $\phi_f$  than EtNAPH [30].

Orange single crystal of MeNAPH was obtained from solvent diffusion method (tetrahydrofuran: n-hexane = 1:3). The crystal and cell structures are shown in Fig. 4. Crystallographic parameters and refinements are listed in ESI Table S1.

As shown in Fig. 4a, the TPA group exhibits a “propeller” shape with the dihedral angle of ~64° which agree well with the geometry optimization results (~68°, ESI Fig. S6). There are two independent

molecules in one cell which are separated in a distance of 9.535 Å and parallel to c-axis (Fig. 4b). A short contact is obvious between two adjacent molecules (ESI Fig. S2). The face-to-face  $\pi-\pi$  stacking interactions exist in adjacent molecules (quasi-intermolecular hydrogen bonds are observed between the C and H with bond length of 2.69, 2.78 and 2.87 Å) and give rise to 2D supramolecular grid structure in compound MeNAPH [31–33].

### 3.2. Application in OLEDs

The morphology of solid film is an important factor for the property of OLEDs using the solution-processed method. The surface morphology of spin-coated films with as-synthesized compounds were investigated by AFM (Fig. 5). The surface roughness of thin films were 0.634, 0.591 and 0.469 nm, respectively, evaluated by the root-mean-square (RMS) roughness. The morphology of the solution-processed thin films were investigate by XRD measurements. As shown in ESI Fig. S7, the films of HT-EMs showed the same patterns as ITO substrate, which indicated the amorphous characters of spin-coated films. As reported, the distinct crystallization issues and defects appeared in the solid film could deteriorate the device efficiency by trapping excitons [34]. Therefore, the interface quenching is negligible in this case.

The simple-structured OLEDs with structure of ITO/PEDOT (20 nm)/HT-EMs (80 nm)/PFN (20 nm)/Al (100 nm) were fabricated with full solution process. As shown in Table 2, the CIE coordinates (ESI Fig. S9) of electroluminescence (EL) shown that the OLEDs were green light emission. The EL photograph and operation mechanism of simple-structured devices were shown in Fig. 6. Noticeably, with the intensity of EL spectra increase steeply with applied driving voltage increased from 5 to 10 V, while the change of EL spectra were negligible. The photoelectric properties of devices were shown in Tables 2 and 3.

The current density vs voltage ( $J-V$ ), luminance vs voltage vs external quantum efficiency ( $L-V-Q$ ) of these devices are shown in Fig. 7. The turn-on voltages ( $V_{\text{on}}$ ) of the device-MeNAPH, device-MeONAPH and device-EtNAPH were 3.0, 2.7 and 3.0 V, respectively (Table 2). The maximum current efficiency (CE) values are in the region of 0.53–0.65 cd A<sup>-1</sup>, maximum luminance ( $L_{\text{max}}$ ) values are in the region of 1114–2010 cd m<sup>-2</sup>. Obviously, the  $V_{\text{on}}$  values are dependent on the difference of HOMO levels between PEDOT:PSS and as-synthesized HT-EMs ( $\Delta E_{\text{inj}}$ , Table 2).

As shown in Fig. 7, the Device-MeONAPH showed highest luminance but lowest efficiency. Therefore, the effects of HOMO level and  $\mu_h$  on the device performance were investigated. The HOMO levels were determined by PYS as shown in Table 1. The  $\mu_h$  was measured with time-of-flight (TOF) technique (ESI Fig. S8) [35,36].

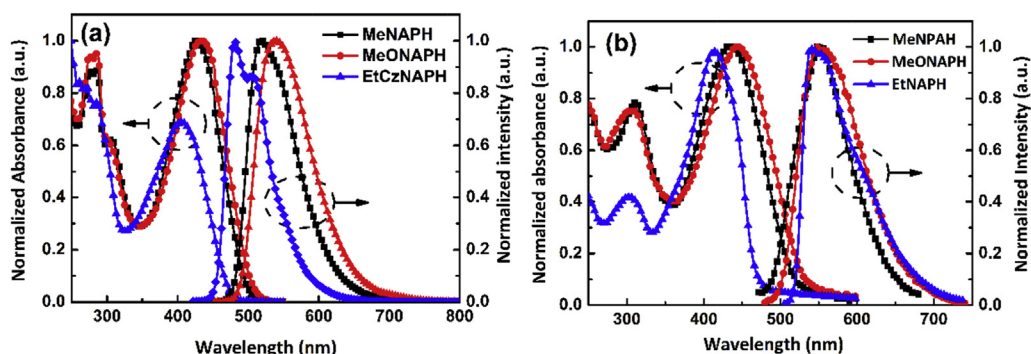


Fig. 2. UV–Vis absorption and PL spectra of as-synthesized HT-EMs: (a) THF solution ( $c = 10^{-5}$  mol L<sup>-1</sup>); (b) solid films.

**Table 1**  
Optical parameters and energy levels of as-synthesized HT-EMs.

	$\lambda_{\max}^a$ (nm)	$\lambda_{\text{on}}^b$ (nm)	PL <sup>c</sup> (nm)	$E_g^d$ (eV)	HOMO <sup>e</sup> (eV)	LUMO <sup>f</sup> (eV)	$\tau^g$ (ns)	$\phi_f^h$ (%)
MeNAPH	427, 435 <sup>i</sup>	497	518, 555 <sup>i</sup>	2.50	−5.34	−2.84	1.805	79.73
MeONAPH	435, 446 <sup>i</sup>	506	539, 548 <sup>i</sup>	2.45	−5.26	−2.81	2.037	88.24
EtNAPH	407, 413 <sup>i</sup>	472	481, 540 <sup>i</sup>	2.63	−5.26	−2.63	1.754	70.56

<sup>a</sup> The maximum absorption peak of UV–Vis was recorded in the  $1.0 \times 10^{-5}$  mol L<sup>−1</sup> THF solution.

<sup>b</sup> The absorption thresholds of UV–Vis.

<sup>c</sup> PL spectra was recorded with excitation wavelength at maximum absorption peak.

<sup>d</sup> Optical energy gaps calculated from the absorption thresholds of UV–Vis absorption spectra according to the equation:  $E_g = 1240/\lambda_{\text{on}}$ .

<sup>e</sup> Measured with photoelectron yield spectroscopy (ESI Fig. S4).

<sup>f</sup>  $|LUMO| = |HOMO| - |E_g|$ .

<sup>g</sup> Fluorescence lifetime recorded in the  $1.0 \times 10^{-6}$  mol L<sup>−1</sup> THF solution (ESI Fig. S5).

<sup>h</sup> Absolute fluorescence quantum yields recorded in the  $1.0 \times 10^{-6}$  mol L<sup>−1</sup> THF solution.

<sup>i</sup> UV–Vis absorption and PL peaks of thin films.

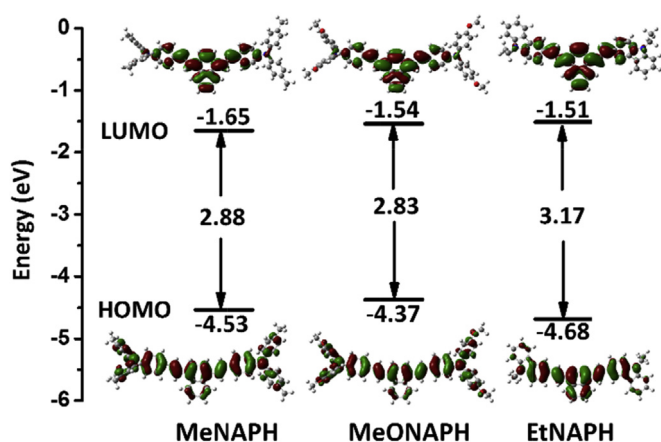


Fig. 3. HOMO and LUMO electron distributions of as-synthesized compounds.

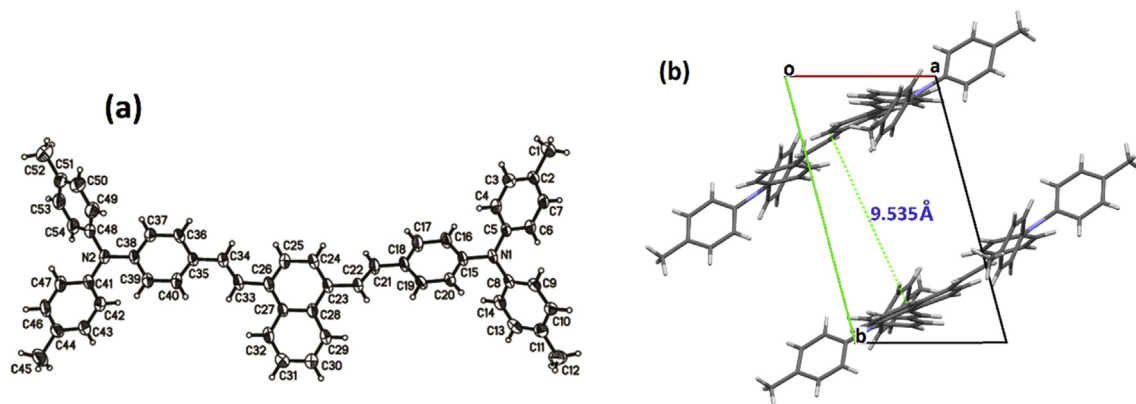


Fig. 4. ORTEP drawing with atom-labelings (a) and crystal cell (b, along the c-axis) of MeNAPH.

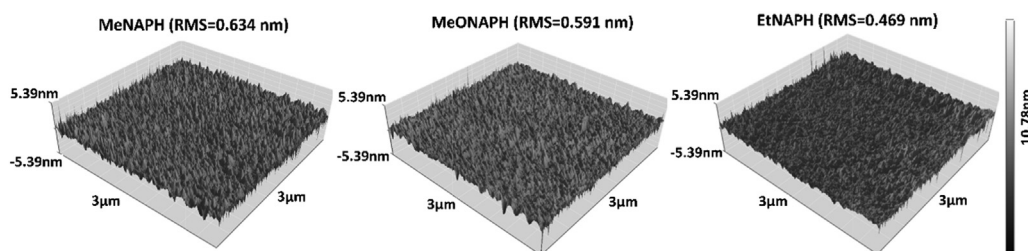


Fig. 5. AFM images of spin-coated thin-films: MeNAPH (RMS = 0.634 nm), MeONAPH (RMS = 0.591 nm) and EtNAPH (RMS = 0.469 nm).

As shown in Fig. 8, the logarithm of hole mobility showed a square root relationship with applied electric field, which followed with the Poole–Frenkel relationship ( $\mu \propto \exp(\beta E^{1/2})$ , where  $\beta$  is the Poole–Frenkel factor and  $E$  is the electric field.) [37]. Obviously, the hole mobility of MeONAPH was higher than that of MeNAPH and EtNAPH when the applied electric fields was in the region of  $1.1 \times 10^5$ – $1.6 \times 10^5$  V cm<sup>−1</sup>. The hole mobilities of MeNAPH, MeONAPH and EtNAPH at applied electric fields of  $\sim 1.5 \times 10^5$  V cm<sup>−1</sup> were  $4.03 \times 10^{-4}$ ,  $4.22 \times 10^{-4}$  and  $3.24 \times 10^{-4}$  cm<sup>2</sup> V<sup>−1</sup> s<sup>−1</sup>, respectively.

As an example, a linear relationship between  $J$  and subtraction of applied voltage ( $V_{\text{app}}$ ) by built in potential ( $V_{\text{bi}}$ ) is observed with  $V_{\text{app}} - V_{\text{bi}} < 0.9$  V in the device-MeNAPH (Fig. 7a). When the  $V_{\text{app}} - V_{\text{bi}} > 5.7$  V, a quadratic relationship is observed. According to above problems, the carrier injection and transition processes can be divided into three stages (Fig. 9 and Table 3).

When in the stage of  $V_{\text{bi}} < V_{\text{app}} < V_{\text{on}}$ , the slope between  $J$  and  $V_{\text{app}} - V_{\text{bi}}$  is close to one (Fig. 7a and Table 3). As reported by J.

**Table 2**  
Photoelectric properties of simple-structured devices.

	$\Delta E_{inj}^a$ (V)	$V_{on}^b$ (V)	$\lambda_{EL}^c$ (nm)	CIE <sup>d</sup>	$L_{max}^e$ (cd m <sup>-2</sup> )	CE <sup>f</sup> (cd A <sup>-1</sup> )	QE <sup>g</sup> (%)	$\mu_h^h$ (cm <sup>2</sup> V <sup>-1</sup> s <sup>-1</sup> )
MeNAPH	0.14	3.0	554	(0.397, 0.573)	1152	0.53	0.20	$4.03 \times 10^{-4}$
MeONAPH	0.06	2.7	556	(0.442, 0.543)	2010	0.54	0.22	$4.22 \times 10^{-4}$
EtNAPH	0.06	3.0	538	(0.342, 0.585)	1114	0.65	0.25	$3.24 \times 10^{-4}$

<sup>a</sup> The difference of HOMO level between PEDOT:PSS and HT-EMs.

<sup>b</sup> Voltage at 1 cd m<sup>-2</sup>.

<sup>c</sup> The wavelength of electroluminescence.

<sup>d</sup> The CIE coordinates of EL spectrum.

<sup>e</sup> The maximum luminance.

<sup>f</sup> Current efficiency at the maximum quantum efficiency.

<sup>g</sup> The maximum quantum efficiency.

<sup>h</sup> The hole mobilities at the electric fields of  $\sim 1.5 \times 10^5$  V cm<sup>-1</sup>.

**Table 3**  
Data of OLEDs operating in the three stages.

	$V_{bi} < V_{app} < V_{on}$			$V_{on} < V_{app} < V_{lmax}$			$V_{lmax} < V_{app}$		
	$V_{app} - V_{bi}^a$ (V)	$\mu^{lowb}$ (cm <sup>2</sup> V <sup>-1</sup> s <sup>-1</sup> )	n <sup>c</sup>	$V_{app} - V_{bi}^a$ (V)	$\mu^{midb}$ (cm <sup>2</sup> V <sup>-1</sup> s <sup>-1</sup> )	A <sup>d</sup> (10 <sup>-7</sup> )	$V_{app} - V_{bi}^a$ (V)	$\mu^{highb}$ (cm <sup>2</sup> V <sup>-1</sup> s <sup>-1</sup> )	n <sup>e</sup>
MeNAPH	<0.9	$2.28 \times 10^{-4}$	1	0.9–5.5	$2.28 \times 10^{-4} - 1.31 \times 10^{-3}$	8.06	>5.5	$>1.31 \times 10^{-3}$	2
MeONAPH	<0.9	$2.42 \times 10^{-4}$	1	0.9–5.0	$2.42 \times 10^{-4} - 1.16 \times 10^{-3}$	3.41	>5.0	$>1.16 \times 10^{-3}$	2
EtNAPH	<1.2	$1.42 \times 10^{-4}$	1	1.2–6.5	$1.42 \times 10^{-4} - 2.21 \times 10^{-3}$	0.58	>6.5	$>2.21 \times 10^{-3}$	2

<sup>a</sup> The subtraction of applied voltage by built in potential.

<sup>b</sup> The hole mobility with the different electric filed.

<sup>c</sup> Fitting by Eq. (1).

<sup>d</sup> Fitting by Eq. (2).

<sup>e</sup> Fitting by Eq. (3).

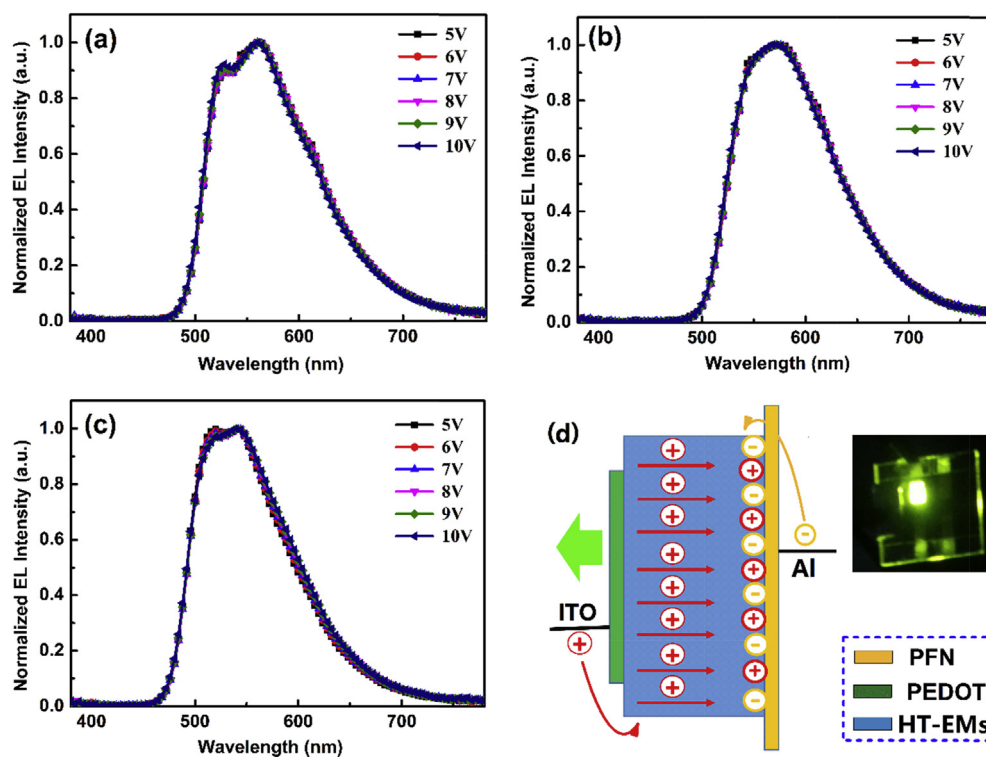


**Fig. 6.** EL spectra ((a) device-MeNAPH; (b) device-MeONAPH; (c) device-EtNAPH) and luminescence mechanism (d) of simple-structured devices.

Staudigel et al., in this step the  $J$  generated from the presence of intrinsic carrier in MeNAPH layer [38]. Therefore, this case was called ohmic current ( $J_{ohmic}$ ) which was dependent on the concentration of carrier in MeNAPH layer ( $p_0$ ), voltage between two electrodes ( $V = V_{app} - V_{bi}$ ), hole mobility with low electric filed ( $\mu^{low}$ ) and thickness of active layer (Eq. (1)).

$$J_{ohmic} = e\mu^{low}p_0 \frac{V_{app} - V_{bi}}{L} \quad (1)$$

In this case, the excitons are not enough for exciting the MeNAPH molecular to emit light. Correspondingly, the luminance ( $L_{EL}$ ) was unobvious in this voltage (Fig. 7b).

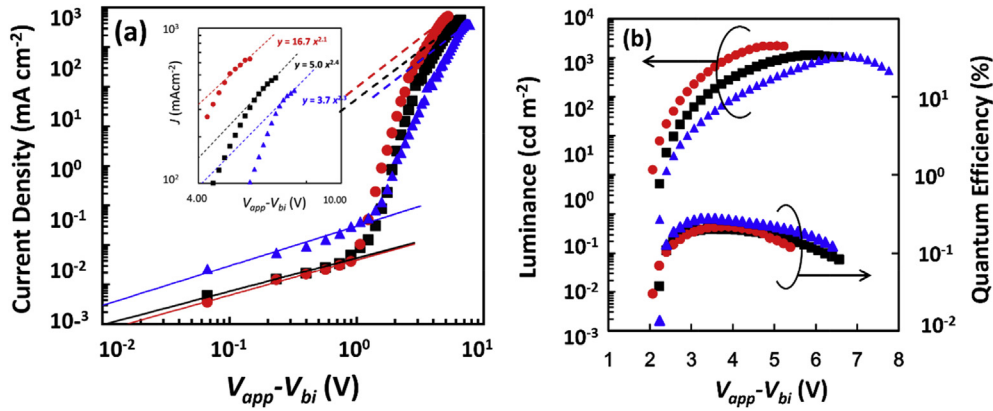


Fig. 7. The current density–voltage ( $J$ – $V$ ) double logarithmic curves, black square for device-MeNAPH, red circle for device-MeONAPH and blue triangle for device-EtNAPH (a), luminance–voltage–quantum efficiency ( $L$ – $V$ – $Q$ ) curves (b) of above devices. (For interpretation of the references to color in this figure caption, the reader is referred to the web version of this article.)

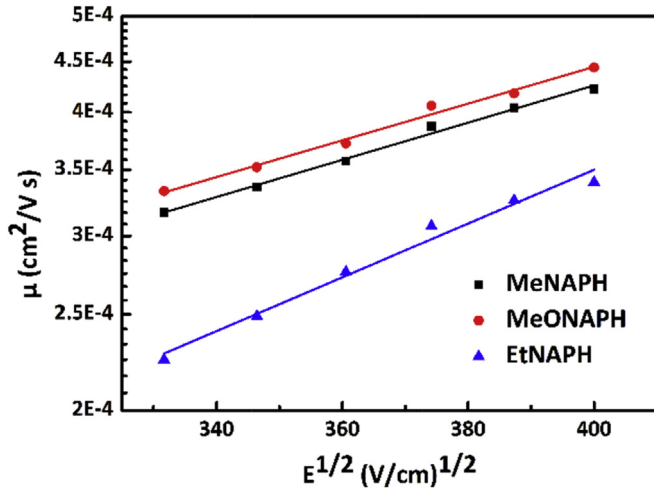


Fig. 8. Hole mobilities plotted with respect to  $E^{1/2}$  for as-synthesized compounds (the solid line is a fit of Poole–Frenkel form).

$$\alpha = \frac{4\pi\sqrt{2m_e}}{h} \quad (2-2)$$

$$E = \frac{V_{app} - V_{bi}}{L} \quad (2-3)$$

Here, the  $A$  is constant,  $q$  elementary charge,  $k_B$  Boltzmann constant,  $\Phi_B$  injection barrier,  $m_e$  the electron mass, and  $h$  Frankel constant. In this case, enough excitons will generate to excite light of MeNAPH layer. This recombination of electron and hole would generate a recombination current ( $J_R$ ), which show a negative direction with the current generate from injection of free carries [40]. The recombination quantum efficiency is dependent on the  $J_R/J$ . As discussed above, the  $J$  should be comprised of  $J_{FN}$  and  $J_R$ , which means the recombination quantum efficiency should be inversely proportional to  $J_{FN}$ .

When  $V_{Lmax} < V_{app}$ , the slope between  $J$  and  $V_{app} - V_{bi}$  is close to two (Fig. 7a and Table 3). This indicates that the concentration of free holes is far exceeding the concentration of filled traps (Fig. 9c), which is defined as the space charge limited current ( $J_{SCLC}$ , Eq. (3)).

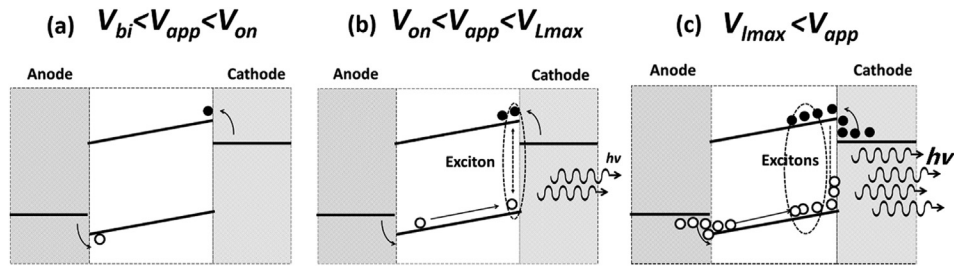


Fig. 9. Three-stage model of carrier injection and transition processes in simple-structured OLEDs.

When  $V_{on} < V_{app} < V_{Lmax}$ , the  $J$  and  $V$  showed an exponential relations (Fig. 7a and Table 3). The steep increase of  $J$  is observed due to the injection of free carriers at high electric field which consisted with the Fowler–Nordheim model (Fig. 9b) (Fitting details see ESI Fig. S10) [39].

$$J_{in} = \frac{Aq^2E^2}{\Phi_B\alpha^2k_B^2} \exp\left(-\frac{2\alpha\Phi_B^{3/2}}{3qE}\right) \quad (2-1)$$

$$J_{SCLC} = \frac{9}{8}\epsilon\epsilon_0\mu^{high}\frac{(V_{app} - V_{bi})^2}{L^3} \quad (3)$$

According to Eq. (3),  $\epsilon$  and  $\epsilon_0$  are the permittivity of MeNAPH and vacuum, respectively. The  $\mu^{high}$  is hole mobility with high electric field,  $L$  the distance between two electrodes,  $V$  the voltage. In this case, the holes are accumulated in the vicinity of Al cathode and resulted in the decrease of luminance.

Device-MeONAPH and device-EtNAPH showed the similar results. The ohmic conduction region for device-MeONAPH and

device-EtNAPH turned up to 0.9 V and 1.2 V, respectively. As shown in Table 1, the LUMO level of MeNAPH (−2.8 eV) is the same as MeONAPH (−2.8 eV). While, the LUMO level of EtNAPH (−2.6 eV) is higher than the other two materials, which means the larger electron injection barrier in device-EtNAPH. This indicated that the electron injection barrier between LUMO level and cathode determined the ohmic conduction region.

Compared to EtNAPH, the hole mobility of MeNAPH and MeONAPH are very similar. Apparently, the  $J$ – $V$  curves exhibit the similar slope when  $V_{on} < V_{app} < V_{lmax}$ . The larger  $\mu^{mid}$  of MeONAPH caused the larger  $J_{in}$  and the lower quantum efficiency in device. The highest external quantum efficiency was observed in device-EtNAPH, which has lowest  $\mu^{mid}$  (Fig. 9b). The relationship between hole mobility and quantum efficiency was consistent with the suspect in the region of  $V_{on} < V_{app} < V_{lmax}$ . In the space charge limited region, the  $J_{SCSL}$  is proportional to the  $\mu^{high}$ . The decrease of quantum efficiency with higher operation voltage resulted from the holes accumulation at the interface of electrodes.

From above analysis, the overlarge operation current from high carrier mobility mainly results in low efficiency. A high efficient carrier-only OLEDs can be realized by choosing multifunctional material with decent carrier mobility to reduce the operation current, high fluorescence or phosphorescence to improve luminance and suitable HOMO, LUMO levels to facilitate charge injection.

#### 4. Conclusions

In this work, three HT-EMs were synthesized and showed good fluorescence quantum yields, suitable HOMO levels, excellent thermal stability and good hole-transporting properties. Fully solution-processed hole-only OLEDs showed the tune-on voltage less than 3 V. The device-MeONAPH exhibited the best parameters of  $L_{max} = 2010 \text{ cd m}^{-2}$ ,  $CE = 0.65 \text{ cd A}^{-1}$  and  $QE = 0.25\%$ . The  $J$ – $V$  curves of these hole-only devices showed three stages obviously. The high  $\mu_h$  showed a positive effect on the  $L_{max}$  but a negative effect on efficiency, because of the overlarge current density during operation. The accumulation of charge led to the efficiency roll-off at high operation voltage.

#### Acknowledgments

The authors gratefully acknowledge the financial support from National High-tech R&D Program (863 Program) (2015AA033402) and Tianjin science and technology plan projects (13ZCZDZX00900). The calculation in this work was supported by high performance computing center of Tianjin University, China.

#### Appendix A. Supplementary data

Supplementary data related to this article can be found at <http://dx.doi.org/10.1016/j.dyepig.2016.03.052>.

#### References

- [1] Tang CW, VanSlyke SA. Organic electroluminescent diodes. *Appl Phys Lett* 1987;51:913–5.
- [2] Jiang Z, Ye T, Yang C, Yang D, Zhu M, Zhong C, et al. Star-shaped oligotriarylamines with planarized triphenylamine core: solution-processable, high- $T_g$  hole-injecting and hole-transporting materials for organic light-emitting devices. *Chem Mater* 2011;23:771–7.
- [3] Han TH, Choi MR, Woo SH, Min SY, Lee CL, Lee TW. Molecularly controlled interfacial layer strategy toward highly efficient simple-structured organic light-emitting diodes. *Adv Mater* 2012;24:1487–93.
- [4] Xue S, Qiu X, Yao L, Wang L, Yao M, Gu C, et al. Fully solution-processed and multilayer blue organic light-emitting diodes based on efficient small molecule emissive layer and integrated interlayer optimization. *Org Electron* 2015;27:35–40.
- [5] Liu ZW, Helander MG, Wang ZB, Lu ZH. Efficient single-layer organic light-emitting diodes based on C545T-Alq<sub>3</sub> system. *J Phys Chem C* 2010;114:11931–5.
- [6] Hu W, Matsumura M. Organic single-layer electroluminescent devices fabricated on CuO<sub>x</sub>-coated indium tin oxide substrate. *Appl Phys Lett* 2002;81:806–7.
- [7] Gross M, Müller DC, Nothofer H-G, Scherf U, Neher D, Bräuchle C, et al. Improving the performance of doped *p*-conjugated polymers for use in organic light-emitting diodes. *Nature* 2000;405:661–5.
- [8] Ho PKH, Kim JS, Burroughes JH, Becker H, Li SFY, Brown TM, et al. Molecular-scale interface engineering for polymer light-emitting diodes. *Nature* 2000;404:481–4.
- [9] Kabra D, Lu LP, Song MH, Snaith HJ, Friend RH. Efficient single-layer polymer light-emitting diodes. *Adv Mater* 2010;22:3194–8.
- [10] Gao WZ, Wang SR, Xiao Y, Li XG. Study on synthesis and properties of novel luminescent hole transporting materials based on *N,N'*-di(*p*-tolyl)-*N,N'*-diphenyl-1,1'-biphenyl-4,4'-diamine core. *Dyes Pigm* 2013;97:92–9.
- [11] Wong W-Y, Ho C-L. Functional metallophosphors for effective charge carrier injection/transport: new robust OLED materials with emerging applications. *J Mater Chem* 2009;19:4457–82.
- [12] Zou Y, Ye T, Ma D, Qin J, Yang C. Star-shaped hexakis(9,9-dihexyl-9H-fluorene-2-yl)benzene end-capped with carbazole and diphenylamine units: solution-processable, high  $T_g$  hole-transporting materials for organic light-emitting devices. *J Mater Chem* 2012;22:23485–91.
- [13] Yasuhiko S, Hiroshi K. Charge carrier transporting molecular materials and their applications in devices. *Chem Rev* 2007;107:953–1010.
- [14] Cao XB, Wen YG, Guo YL, Yu G, Liu YG, Yang LM. Undoped, red organic light-emitting diodes based on a *N,N,N',N'*-tetraphenylbenzidine (TPD) derivative as red emitter with a triphenylamine derivative as hole-transporting layer. *Dyes Pigm* 2010;84:203–7.
- [15] Zhao XM, Wang SR, You J, Zhang YT, Li XG. Solution-processed thermally stable amorphous films of small molecular hole injection/transport bifunctional materials and their application in high efficiency OLEDs. *J Mater Chem C* 2015;3:11377–84.
- [16] Liu XC, You J, Xiao Y, Wang SR, Gao WZ, Peng JB, et al. Film-forming hole transporting materials for high brightness flexible organic light-emitting diodes. *Dyes Pigm* 2016;125:36–43.
- [17] Zhu M, Ye T, Li C-G, Cao X, Zhong C, Ma D, et al. Efficient solution-processed nondoped deep-blue organic light-emitting diodes based on fluorene-bridged anthracene derivatives appended with charge transport moieties. *J Phys Chem C* 2011;115:17965–72.
- [18] Zou Y, Zou J, Ye T, Li H, Yang C, Wu H, et al. Unexpected propeller-like hexakis(fluorene-2-yl)benzene cores for six-arm star-shaped oligofluorenes: highly efficient deep-blue fluorescent emitters and good hole-transporting materials. *Adv Funct Mater* 2013;23:1781–8.
- [19] Sheldrick GM. A short history of SHELX. *Acta Cryst* 2008;64:112–22.
- [20] Dolomanov OV, Bourhis LJ, Gildea RJ, Howard JAK, Puschmann H. OLEX2: a complete structure solution, refinement and analysis program. *J Appl Cryst* 2009;42:339–41.
- [21] Frisch MJ, Trucks GW, Schlegel HB, Scuseria GE, Robb MA, Cheeseman JR, et al. Gaussian 03, revision E. 01. Wallingford, CT: Gaussian, Inc.; 2004.
- [22] Li K, Qu J, Xu B, Zhou Y, Liu L, Peng P, et al. Synthesis and photovoltaic properties of novel solution-processable triphenylamine-based dendrimers with sulfonyldibenzene cores. *New J Chem* 2009;33:2120–7.
- [23] Jolt Oostraa A, Blom PWM, Michels JJ. Prevention of short circuits in solution-processed OLED devices. *Org Electron* 2014;15:1166–72.
- [24] Karthikeyan CS, Thelakkat M. Key aspects of individual layers in solid-state dye-sensitized solar cells and novel concepts to improve their performance. *Inorg Chim Acta* 2008;361:635–55.
- [25] Neogi I, Jhulki S, Rawat M, Anand RS, Chow TJ, Moorthy JN. Organic amorphous hole-transporting materials based on Tröger's Base: alternatives to NPB. *RSC Adv* 2015;5:26806–10.
- [26] Gao WZ, Wang SR, Xiao Y, Li XG. Synthesis and properties of new luminescent hole transporting materials containing triphenylamine and carbazole units. *Spectrochim Acta A* 2012;98:215–21.
- [27] Mimaite V, Ostrauskaite J, Gudeika D, Grazulevicius JV, Jankauskas V. Structure-properties relationship of hydrazones containing methoxy-substituted triphenylamino groups. *Synth Met* 2011;161:1575–81.
- [28] Hisao I, Daisuke T, Tamotsu S, Nobuyuki S, Yasuo K, Michio N. Photoelectron yield spectroscopy for electronic structures of organic electronic materials and their interfaces. *Surf Sci* 2007;28:264–70.
- [29] Nakahara K, Mitsui C, Okamoto T, Yamagishi M, Matsui H, Ueno T, et al. Furan fused V-shaped organic semiconducting materials with high emission and high mobility. *Chem Commun* 2014;50:5342–4.
- [30] Lu T, You J, Zhao D, Wang H, Miao Y, Liu X, et al. Synthesis of novel s-triazine/carbazole based bipolar molecules and their application in phosphorescent OLEDs. *J Mater Sci Mater Electron* 2015;26:6563–71.
- [31] Subeesh MS, Shanmugasundaram K, Sunesh CD, Won YS, Choe Y. Utilization of a phenanthroimidazole based fluorophore in light-emitting electrochemical cells. *J Mater Chem C* 2015;3:4683–7.
- [32] Rozycka-Sokolowska E, Marciniak B, Kosik S, Dondela B, Bak Z. Two isostructural halogen derivatives of 9-ethylcarbazole: crystal structure, Hirshfeld surface analysis, and structural comparison with other simple analogs. *Struct Chem* 2015;26:873–86.
- [33] Mulani S, Xiao M, Wang S, Chen Y, Peng J, Meng Y. Structure properties of a highly luminescent yellow emitting material for OLED and its application. *RSC*

- Adv 2013;3:215–20.
- [34] Lin WC, Lin HW, Mondal E, Wong KT. Efficient solution-processed green and white phosphorescence organic light-emitting diodes based on bipolar host materials. *Org Electron* 2015;17:1–8.
- [35] Cusumano P, Gambino S. Space charge and carrier trapping effects on the transient photocurrents of organic materials using the time-of-flight technique. *J Electron Mater* 2007;37:231–9.
- [36] Ma X, Wang S, Li X, Xiao Y. Thermally induced crystallization behavior and film microstructure alteration of *N,N,N',N'*-tetraphenylbenzidine (TPB) and *N,N,N',N'*-tetra-*p*-tolyl-benzidine (TTB). *Org Electron* 2014;15:1876–83.
- [37] Liao YL, Hung WY, Hou TH, Lin CY, Wong KT. Hole mobilities of 2,7- and 2,2'-disubstituted 9,9'-spirobifluorene-based triaryldiamines and their application as hole transport materials in OLEDs. *Chem Mater* 2007;19:6350–7.
- [38] Staudigel J, Stößel M, Steuber F, Simmerer J. A quantitative numerical model of multilayer vapor-deposited organic light emitting diodes. *J Appl Phys* 1999;86:3895.
- [39] Lampert MA, Mark P. *Current injection in solids*. Academic Press; 1970.
- [40] Konezny SJ, Smith DL, Galvin ME, Rothberg LJ. Modeling the influence of charge traps on single-layer organic light-emitting diode efficiency. *J Appl Phys* 2006;99:064509.